Revision 2 - Experimental study of phlogopite reaction rim formation on olivine in phonolite melts: kinetics, reaction rates and residence times.

Thomas Bartholomew Grant[1,2], Ralf Milke[1], Bernd Wunder[2], Richard Wirth[2] and Dieter Rhede[2]

1 Institut für Geologische Wissenschaften, Freie Universität Berlin, Malteserstrasse 74-100, 12249 Berlin, Germany

2 GeoForschungsZentrum Potsdam, Telegrafenberg, 14473 Potsdam, Germany

ABSTRACT

Experiments were conducted to reproduce reaction rims of phlogopite ± diopside around olivine that have been observed within a wide range of potassic melts, including phonolite. Phlogopite is also a common secondary phase formed at the expense of olivine during metasomatic events involving K_2O and H_2O rich fluids or melts. Piston cylinder experiments where olivine single crystals were reacted with synthetic phonolite melt at 10.7-14.7 kbar and 950-1000ºC recreate the mineralogy and textures documented in natural samples. Rim growth is parabolic with time, indicating a diffusion-controlled reaction. Fast diffusion in the melt and varying compositions across the phlogopite reaction rims suggest that diffusion through the rims, along grain boundaries is rate limiting. Reaction rates dramatically increase with temperature as well as the bulk water content of the sample charge. This is because of increasing amounts of atomically bound hydrous species along the grain boundaries increase the rates of diffusion and thereby the rates of rim growth. Atomically bound

hydrous species increase the rates of rim growth by lowering the activation energy for diffusion and by increasing the solubility of diffusing species in the grain boundary region. Transmission electron microscopy shows the presence of isolated pores and open grain boundaries. Most of these may have opened during quenching but there is some evidence to suggest that a free fluid phase may have been locally present in experiments with high melt water contents (>8 wt.%). The measured rim growth rates at different conditions are used to estimate residence times of reacting olivine crystals in natural systems.

Keywords: Phlogopite, olivine, reaction rims, grain boundary diffusion, metasomatism

INTRODUCTION

Phlogopite bearing peridotite rocks has been identified in a number of locations; the Ivrea Zone, Southern Alps (Zanetti et al 1999; Grieco et al, 2001), the Horoman peridotite complex (Arai and Takahashi, 1989), and Lherz (Bodinier et al, 2004). Additionally, phlogopite bearing peridotite xenoliths are observed (Aoki, 1975; Lloyd et al, 1991; Wulff-Pedersen et al, 1996; Stiefenhofer et al, 1997). The phlogopite, along with other phases, is often secondary and forms at the expense of primary peridotite phases such as olivine during metasomatic events involving K_2O and H_2O rich melts or fluids. Clear evidence of replacement of olivine by phlogopite was described in the Horoman peridotite complex (Arai and Takahashi, 1989). The origin and composition of the fluids or melts involved in these reactions are not always well constrained. Slab derived melts or fluids (Sudo and Tatsumi, 1990; Zanetti et al 1999; Prouteau et al, 2001, Wunder and Melzer, 2003), partial melting of pre-metasomatised

mantle (Grieco et al, 2001; Thibault et al, 1992) and fluids released from fractionating alkali basaltic melts (Arai and Takahashi, 1989) have been suggested as potential sources. The range in pressures and temperatures of phlogopite formation are also potentially very large. Xenolith samples from Bultfontein Floors (Aoki, 1975) are thought to originate from 170-100 km compared with much shallower conditions in the Horoman peridotite complex (Arai and Takahashi, 1989) and the Ivrea Zone (Grieco et al, 2001). The stability field of phlogopite has been shown to extend deep into the mantle (Trønnes, 2002) making it an important reservoir for volatiles, alkalis and trace elements. Phlogopite, may also be an important phase in the genesis and alkali budget of arc magmas (Sudo and Tatsumi, 1990), intraplate magmas (Pilet et al, 2011) and ultrapotassic melts (Foley, 1992) during partial melting of metasomatised mantle. Therefore, the mechanisms by which phlogopite forms at the expense of upper mantle minerals is of particular interest.

In addition, there are numerous examples of olivine xenocrysts that have reacted to form phlogopite ± diopside reaction rims when in contact with K_2O and H_2O rich melts such as: lamprophyre (Foley et al, 2002; Semiz et al, 2012), lamproite (Carmichael, 1967; Çoban and Flower, 2006), kimberlite (Neal and Taylor, 1989), minettes (Davis and Smith, 1993), nephelinite – leucitite (Lloyd et al, 2002) as well as phonolite (Henderson et al, 2012, Grant et al, 2013). These are very small-scale analogues of metasomatic reactions and in all these cases olivine cores clearly show textures indicative of dissolution and replacement by phlogopite. Phase relationships of potassic melts show a change in liquidus phases from olivine to phlogopite ± diopside during cooling (Luth, 1967; Arima and Edgar, 1983; Draper and Green, 1997).

In this study we experimentally reacted olivine single crystals with synthetic

phonolite melt to form phlogopite ± diopside reaction rims. This simple experimental setup recreates the textures and mineralogy observed in naturally occurring rims formed between olivine and phonolite (Henderson et al, 2012; Grant et al, 2013) and other similar melts. The dissolution of olivine and precipitation of phlogopite is driven by a combination of diffusion and interface kinetics, where the slower of the two is rate-limiting (see Dohmen and Chakraborty, 2003 for a detailed discussion). We find that the rate limiting process is grain boundary diffusion through the phlogopite reaction rims. We therefore investigate the structural properties of grain boundaries and interphase boundaries using transmission electron microscopy (TEM). The influence of pressure, temperature and bulk H_2O content of the melt on reaction rim growth rates is also discussed. The primary aim of this work is to use experimentally derived rim growth rates to estimate residence times of olivine xenocrysts in the Heldburg Phonolite described by Grant et al (2013). These can then be applied to other occurrences of phlogopite rim growth on olivine in K_2O and H_2O rich melts.

EXPERIMENTAL METHODS

Starting materials

Two Fe-free synthetic phonolite glasses were prepared (PHG2 and PHG3). The compositions of these two glasses are given in Table 1. Oxide and carbonate forms of each component were accurately weighed, crushed in an agate pestle and mortar in ethanol, and then placed into a platinum crucible. The mixture was then heated in a box furnace at 1600ºC for >24 hrs to create a homogenous melt. The melt was then quenched in water to form a glass, removed and checked for homogeneity before

being crushed and used in experiments. PHG3 is a Ca-free glass, which was used in experiments to avoid liquidus diopside that formed in experiments using PHG2 (see later). Both starting material glasses were reasonably homogenous (see Table 1). PHG2 experienced little alkali loss. PHG3 lost ~1 wt.% Na during analysis, accounting for its low total. Quench rates were fast enough to inhibit micro-crystals in both PHG2 and PHG3. We used pure forsterite from a single crystal synthesized by IKZ Berlin and a single crystal of San Carlos olivine. Fragments of each were then crushed dry using a metal pestle and mortar, separated under size intervals of >500 μm, 250- 500 μm and <250 μm and the middle size grouping was used for experiments. Olivine grains were then added to the crushed glasses of PHG2 or PHG3 in ratios of 84:16 wt.% (glass : forsterite / San Carlos). The composition of the San Carlos olivine is given in Table 1. Platinum capsules with lengths of about 6mm, diameters of 3 mm, and wall thicknesses of 0.3 mm were used for all experiments. One end was crimped and then welded using a PUK3 arc welder. Double distilled water was added via micro-syringe, and then followed by the forsterite-glass (or San Carlos-glass) mixture in proportions to give the desired bulk water contents. The top of the capsule was then welded, weighed and then placed in a 100°C oven for around an hour and then weighed again to check for any weight loss and the quality of the welded seal. Samples that showed no weight loss were then used. Capsules were also cleaned and weighed after the experiments to check for any weight loss. No samples showed any loss of weight after the experiments, indicating that no volatiles were lost at peak run conditions. Sample names, bulk water contents, estimated melt water contents (based on an assumed 84:16 ratio), and run conditions (P-T-t) are given in Table 2. Three sets of time series experiments were conducted with three different bulk water contents of 3.9-4.2 wt.% (low water), 5.6-6.5 wt.% (medium water) and

126 7.2-8.0 wt.% (high water).

127

128 **Piston cylinder apparatus**

129 All experiments were conducted using a Johannes type piston cylinder apparatus (see
130 Johannes et al, 1971; and Johannes, 1973). The sample charge consisted of a drilled
131 natural CaF_2 holder for two capsules and the Ni/Ni-Cr thermocouple that measured
132 the temperature at the middle of the capsules. This was surrounded by a graphite
133 sleeve (furnace), and then encased in a 1 inch wide drilled natural CaF_2 outer part.
134 Friction effects were accounted for due to the use of natural CaF_2 pieces (Harlov and
135 Milke, 2002). Loading of pressure was done first and then the temperature was
136 increased to the peak conditions. Pressure stayed constant to within 0.2 Kbar and the
137 measured thermocouple temperature to within 2-3°C during the experiments.
138 However there could be small thermal gradients across the samples, but the ΔT across
139 the sample is unlikely to be more than 20°C (Schilling and Wunder, 2004). Samples
140 were quenched at a rate of ~20°C/s (calculated over a temperature range of 950-
141 450ºC). Run conditions for all experiments are given in Table 2. We conducted two
142 sets of experiments. Single series experiments tested a wider range of different
143 temperatures, pressure, water content, duration and olivine composition, and time
144 series experiments where all parameters were kept constant except for the run
145 duration.

146

147 **ANALYTICAL METHODS**

148 **Electron microprobe (EMP)**

149 An initial assessment of all samples was conducted using the JEOL JXA-8200
150 (Superprobe) at FU Berlin, Geocampus. Back-scattered electron (BSE) images were

taken as well as microprobe analysis of reaction rims and host olivines. Some data was collected for glasses using wide beams of 15 μm to limit loss of alkalis compared to fully focused beams for all other phases. All analyses were made with accelerating voltages of 15 kV, 20 nA beam current and counting times of 10s on peak and background. The same analytical conditions but with focused beams of 1μm were used to make a series of line scans on SC31. Analyses of glasses were taken using a JEOL (Hyperprobe) JXA-8500F with a thermal field emission cathode (FEG) at GFZ Potsdam. The analysis of glass posed a significant problem considering the high alkali content (>14 wt.%), high volatile contents and the presence of small crystals of phlogopite throughout the glass. In order to measure profiles through glasses away from reaction rims with the maximum spatial resolution (i.e. distance between each point) whilst minimizing migration of alkalis, specific conditions used were; 5 nA beam current, an accelerating voltage of 6 kV, short counting times of 10s on peak and background with a defocused beam of 5 μm. Standards included jadeite (Si and Na), periclase (Mg), orthoclase (Al and K).

Rim thickness measurements

Using the BSE images from the microprobe, rim thicknesses were measured. For each sample several rims were measured, giving >20-30 data points of rim thickness. These were then averaged to give the estimated rim thickness for each sample. Due to the uncertainty in the orientation of the reaction rim with respect to the polished surface, some rims could be cut at a low angle, making their thicknesses appear larger than they actually are. This means that the observed thickness is always slightly larger than the actual rim thickness (Liu et al, 1997). For this reason, the best locations for thickness measurements were where the rims were generally thinner. Rim thicknesses

are comparable from different experiments as long as the same method of measuring rim thickness is always used.

Transmission electron microscope (TEM)

TEM foils were prepared using the focused ion beam (FIB) techniques described by Wirth (2004). Two foils were cut on sample TSF2, one perpendicular to and crossing the olivine-phlogopite interface (foil #3259), and one cut parallel to the olivine interface through the phlogopite rim (foil #3281). One foil was cut from sample TSF6 that was perpendicular to and crossed the olivine –phlogopite interface. Two further foils (#3518 and #3520) were then cut in sample TSF 8, both were perpendicular to the olivine interfaces. TEM and HRTEM images were taken using the FEI Tecnai G2 F20 X-Twin transmission electron microscope at GFZ Potsdam. EDX analyses were acquired using the EDX detector. High angle annular dark field (HAADF) scanning transmission electron microscopy (STEM) images were also taken.

RESULTS

Reaction rim assemblages and textures

In all experiments the olivine (Forsterite or San Carlos) reacted with the melt. The Ca-bearing melt (PHG2) produced inner rims of phlogopite and an overgrowth of diopside (Figure 1b) with diopside also occurring as a liquidus phase. The Ca-free (PHG3) experiments produced phlogopite rims only (Figure 1c). These rim assemblages are consistent with those observed in natural examples (Figure 1a). Reaction rims could not be formed at water contents lower than around 4 wt.% bulk H_2O. One Ca-bearing experiment at 1000°C produced rims of more Mg-rich olivine

around olivine in part of the capsule, but phlogopite-diopside double rims in the rest of the capsule. This reflects a small thermal gradient across the samples, where at 1000°C olivine is stable in the melt, and is consistent with the phase relationships of Draper and Green (1997). At just below 1000°C phlogopite rims are stable, consistent with the experiments at 950°C. In the Ca-free melt single rims of phlogopite grew around olivine crystals and no diopside formed. Phlogopite was a liquidus phase in these experiments. Representative BSE images of the reaction rims are shown in Figure 1. Olivine shows classic dissolution textures of convoluted and lobate crystal edges in contact with the phlogopite reaction rim. These features are commonly observed in reaction rims (for example, Coombs and Gardner, 2004). Rim grain sizes vary but are mostly 5-15 μm. Grain sizes tend to increase with increasing run duration. All rims contain some small black patches in Figure 1b-c, which are likely to have formed during polishing and plucking of rim grains. TEM foils were chosen at locations where these were not present in order to avoid sampling areas that might have been affected by plucking. Diopside in Ca-bearing experiments does not always form a continuous rim around phlogopite inner rims and diopside crystals are separated by melt. Diopside forming around phlogopite rims appears to be a local effect of preferential nucleation as Grant et al (2013) suggest.

Despite the high water contents used in the experiments, the melts did not become saturated with fluid. One experiment (TSF12) did show some vesicles in the melt surrounding reaction rims, but as several experiments at higher bulk H_2O did not show the same features, the vesicles could have been formed during quenching. There is also little evidence of crystal settling in the experiments. High water contents are known to be soluble in phonolite melts even at low-pressure conditions (Carroll and Blank, 1997; Schmidt and Behrens, 2008).

Reaction rates

Measured rim thicknesses for the time series experiments in Ca-free melt were plotted against the square root of time (Figure 2a-b). Rim growth is not linear with time. For all three different water contents rim growth is parabolic with time, indicating a diffusion-controlled reaction. Rim growth increases with increasing water content in the melt. We can express this behavior with a parabolic rate law (with units of m^2/s) for each range in water. This was calculated from the slope of the trend lines given in Figure 2a-b. This gives values of 3.24×10^{-16} m^2/s for high water contents (~8 wt.% H_2O), 4.3×10^{-16} m^2/s for intermediate water contents (~5.7 wt.% H_2O) and 6.99×10^{-16} m^2/s for the lowest water contents (~4 wt.% H_2O). To further explore the effects of water on the rim growth we looked at the experiments in Ca-bearing melt. For each sample the rim thickness was measured in the same way as before (only measuring the phlogopite inner rims) and it was assumed that parabolic rim growth occurred in all experiments. For each experiment at 950ºC the measured rim growth was divided by the square root of time. The results of this are shown in Figure 2c. The Ca-bearing and Ca-free melt experiments are consistent with each other despite differences in melt composition, and therefore phase relations, host olivine composition (San Carlos or forsterite), and pressure (10 or 14 kbar). The bulk H_2O content and temperature have a large impact on the rim growth whereas small differences in melt composition, pressure and olivine composition do not. Figure 2c shows that there is a linear relationship between log (m^2/s) and H_2O content.

TEM results

Phlogopite-phlogopite grain boundaries

For experiments at around 6 wt.% H_2O the majority of grain boundaries do not appear to have any open space or non-crystalline material between phlogopite crystals. HRTEM imaging shows that the lattice fringes of adjacent phlogopite crystals touch (Figure 3c). This means that the grain boundaries are closed, at least to the scale of ~1 nm. Some grain boundaries appear to have open cavities that are planar and follow crystal edges (Figure 3a). These often contain some epoxy material introduced during polishing but no other precipitated material was observed in the open grain boundaries observed. There are also grain boundaries that contain small micro-pores (<400 nm) (Figure 3b). These pores are oblong to elongate and curved but are separated by regions of grain boundaries where lattice fringes touch, indicating no open grain boundary space connecting different pores. However, the ability to observe 3D connectivity of pores over large enough scales using TEM is not possible Therefore, from what can be viewed by TEM, it is unlikely that a connected open grain boundary network exists between micropores.

At higher H_2O contents of around 8 wt.% there appears to be a higher density of open linear, to slightly curved, grain boundaries around (greater or equal to) 10 nm wide. These can terminate at crystal edges or taper out along a grain boundary. Pores are present at most grain boundaries and these can be up to 100 nm (Figure 3d) or very small nm sized pores along a grain boundary (Figure 3e). The pores in the latter case are much closer together than those seen in experiments with less water (Figure 3b). For all analyzed TEM foils, rim phlogopites do not appear to be orientated in one crystallographic direction and show random orientations throughout the reaction rims.

Phlogopite-olivine interphase boundaries

At intermediate water contents (6 wt.%), olivine-phlogopite interphase boundaries are

typically closed with few pores and often the lattice fringes of olivine and phlogopite touch (Figure 4a). Open pore cavities are present in some locations (Figure 4b). Although only a small section of the olivine-phlogopite interface was captured by the TEM foil the presence of pores was not limited to being at the head of finger like projections, reported by Milke et al (2013) for quartz-orthopyroxene interphase boundaries into olivine, but can occur anywhere along the rim. This does not contradict their mechanism but shows that other processes might also be involved. Olivine surfaces appear rounded at large magnifications but at low magnifications crystal facets in the dissolving olivine are created (Figure 4). The irregular shape of the interface suggests that the dissolution of olivine is not necessarily faster at different crystal planes or orientations. There is also no correlation between the orientations of phlogopite with that of the host olivine.

At higher water contents the olivine-phlogopite interphase boundaries are clearly open (Figure 4c-d). The open space between olivine and the phlogopite rim is planar and between 40-50 nm wide. HRTEM shows that there are several zones of different material at the olivine side of this interphase boundary (Figure 5). From the open interphase boundary to the interior of the host olivine crystal 3 different zones are identified: an amorphous Si-rich surface layer (ASSL), a distorted olivine region and a finally an undistorted olivine region. The ASSL is around 8 nm thick and is consistent with the ASSL observed on olivine by Daval et al (2011) and other phases (Hellmann et al, 2012, Daval et al, 2013). Due to the small size of the ASSL it was not possible to obtain quantitative data on their composition.

The first 40 nm of the olivine crystal at the interface appears to be distorted. The distortions in the olivine lattice were observed as irregular lattice fringes giving a mottled texture and broader diffraction spots (see figure 5). The distorted region

typically has a regular and nearly planar interface with the ASSL. Daval et al (2011) also noted that olivine adjacent to interfacial regions can be distorted. The distorted region is non-stoichiometric as its Mg / Si ratio is <2 (Table 3), but it is also apparently depleted in Si relative to the non-distorted olivine (Figure 5b). The distorted region most likely has a lower density than the non-distorted olivine, as Mg and Si are both removed during dissolution. Pokrovsky and Schott (2000) showed that the initial stages of dissolution of olivine in acidic solutions are incongruent with M^{2+} (Mg^{2+}, Fe^{2+}) released more rapidly than silica, resulting in an ASSL. Such a dissolution mechanism was also predicted from ab initio quantum mechanical calculations (Liu et al, 2006). Our data are consistent with such a model. The boundary between distorted and non-distorted olivine is irregular.

Melt pockets

No melt films were observed in any of the TEM foils but melt pockets within the reaction rims were observed (Figure 6). These melt pockets are not common and do not appear to be connected by melt films along the grain boundaries, indicating a low degree of wetting. The melt pockets can vary in size from 1 μm to several nm. In one case we see an area of amorphous material next to an open cavity (Figure 6a). Semi-quantitative EDX analyses of melt pockets showed that their compositions showed enrichments in both Si and Al with minor K and Mg. This would be the expected composition of the bulk melt if isolated and then fractionated phlogopite, except for the absence of Na. Due to short counting times it is unlikely that all the Na would have been volatilized even though there was some beam damage after the analyses, which also reflects the hydrous nature of the melts. The Na could have been fractionated into the phlogopite but seeing as the Na content of phlogopites is very

low this also seems unlikely too. Alternatively, Na could be partitioned into a fluid phase (if present) or it is highly mobile through the reaction rims and can diffuse rapidly to the melt.

Chemistry

Melt profiles

Two samples, TSF4 (black circles) and TSF6 (grey circles), with intermediate bulk H_2O contents were analyzed to see if there were any concentration profiles in the melt (Figure 7). For each sample, 4 line scans were taken parallel to each other. The locations of the line scans were taken in regions of glass that were free of other olivines to avoid the possibility that profiles from nearby reactions overlap. Step sizes of 5 μm were used to avoid further loss of alkalis by damaging an area of glass by multiple analyses. This was a noticeable problem when step sizes were lower. Due to the presence of crystals within the glass, mixed analyses were common. This was especially problematic for TSF4, and is why the MgO profile is much more irregular than for TSF6. Data points with anomalously lower SiO_2, and higher MgO than the majority of glass analyses were then removed from the data set, but there are still many which could be affected by small fractions of phlogopite in the analyses. For each sample, all four line scans were then compiled together into a single profile. The results of this are shown in Figure 7. The error bars for Na_2O and K_2O are large because of the short counting times needed to reduce loss of alkalis.

All elements (Si, Al, Na and K) except for Mg have very similar concentrations as the starting material glass within the error bars of the analyses. This is the same for both samples. Magnesium contents in the glasses (<1 wt.%) are significantly lower than the starting material (1.9 wt.%, taking into account the water content of the

351 melt). All elements show homogenous distribution throughout the line scans within
352 the error of the analyses. The closest point to the reaction rims has the same
353 composition as the melt >300 μm away from the rims. Calculating the differentiation
354 in the melt with different amounts of phlogopite can produce the same melt
355 compositions and the depletion in MgO with around 2-3% phlogopite formation. The
356 low totals of the analyses (around 92%) reflect the high concentration of volatiles in
357 the melt and are consistent with the amounts of water added, just under 7 wt.% by
358 melt (5.7 wt.% by bulk of the sample). Note that the water content of phlogopite
359 (ideally 4.3 wt.%) is lower than that of melt in most of the experiments (including
360 those where line scans were taken). Therefore the water content of the melt should
361 increase slightly as phlogopite crystallizes.
362
363 *Reaction rim profiles*
364 One sample (SC31) was chosen for a detailed analysis of the distribution of elements
365 throughout the phlogopite reaction rims. This sample was a good choice for this study
366 because the reaction rims were large, and due to the presence of Fe, Ni and Ca, this
367 sample allowed investigation of a wider range of elements during reaction. Six line
368 scans were taken from the olivine through the rim and into the melt. Melt analyses
369 were then removed as the focused beams caused significant damage. The presence of
370 small diopside crystals in the rims caused a large number of mixed analyses. These
371 were easily spotted by higher CaO contents in the rim phlogopite data. We placed a
372 cut off point and removed all phlogopite data points with >0.15 wt.% CaO. All line
373 scans were then collated together into one single profile for each element. The results
374 of the rim profiles are given in Figure 8. The dashed lines in Figure 8 show the
375 location of the interface between olivine and phlogopite.

The profiles for SiO_2 show a constant concentration in the olivine (over a distance of nearly 20 μm) right up to the reaction interface and then a step jump at the rim. The inner rim is then constant in SiO_2 composition for several microns and then becomes very irregular towards the outer rim. The distribution of K_2O is constantly low in the olivine and then increases over several microns, corresponding to mixed analyses across the olivine-rim interface. Throughout the rim K_2O is relatively constant. Both FeO and MgO show very homogenous concentrations in the host olivine right up to the rim interface. The rims are slightly enriched in both components in the inner rims near the olivine and become depleted in both elements towards the melt. For Na_2O and CaO, the overall contents are very low in both olivine and the reaction rims and the short counting times mean that their analyses carry large errors. This makes it difficult to observe any real trends in these components. However, they do not appear to vary across the reaction rims significantly. The profile for Al_2O_3 shows a consistent and strong variation throughout the phlogopite rim, being higher in concentration near the melt interface compared to near the olivine interface. Finally, for NiO, despite the low overall abundances, there does appear to be a consistent trend of decreasing NiO with distance from the olivine. Table 4 includes some representative data of phlogopite compositions from these line scans. Phlogopite compositions at the olivine interface contain excess octahedral Mg, 3.2 p.f.u. (per formula unit), compared to phlogopite at the melt interface with Mg of 2.8 p.f.u. Some Mg can be tetrahedrally coordinated in micas in Al and Fe deficient systems (Seifert and Schreyer, 1971). Increasing Al (up to 1.1 Al p.f.u.) and decreasing Mg (2.8 Mg p.f.u.) towards the melt interface indicates some octahedrally coordinated Al. Towards the melt interface there is a general increase in Al, K, Si and Na p.f.u. in phlogopite.

401

402 **DISCUSSION**

403 **Reaction mechanisms**

404 *Diffusion mechanism*

405 The results of the time series experiments show that the rim thicknesses have a linear
406 relationship with the square root of time, i.e. parabolic rim growth. This is a strong
407 indication that rim growth rates are controlled, or rate limited, by a diffusion process.
408 It is therefore important to discuss where diffusion is rate limiting. There are several
409 possible phases through which diffusion could be rate limiting: the melt, the
410 polycrystalline reaction rims (phlogopite) or the host olivine.

411 We see no evidence of any concentration profiles in major elements (for
412 example Mg-Fe zoning) forming in the host olivines, which remain homogenous over
413 10s of microns throughout the reaction. Therefore the reaction process must outpace
414 volume diffusion of elements within olivine. Element profiles through the glass do not
415 show any signs of concentration profiles as well. The melt is homogenous over
416 distance >300 μm and right up to the reaction rim interface, within the resolution of
417 the analyses. For phlogopite to continually form there must be a supply of elements
418 from the melt. The step profiles imply that diffusion in the melt must be fast. Most
419 elements in the glass remain similar to the host melt, whereas MgO shows significant
420 depletion. The homogenous depletion of MgO throughout the melt could only have
421 formed if the diffusion rates in the melt were fast. Secondly, although there is little
422 data on element diffusion rates in phonolites, diffusion rates in wet rhyolite melts for
423 Na (from Zhang et al 2010) are fast enough to equilibrate over the time and length
424 scales of the experiments. Furthermore, the diffusion of elements in the melt will be
425 related to the viscosity of the melt. Adding water will reduce the viscosity and

426 therefore increases the diffusion rates, but this effect is most pronounced at low water
427 contents, where OH- acts as a network modifier, and then reduces at higher water
428 contents. This is inconsistent with the exponential increase in reaction rates with
429 increasing water contents. It is therefore most likely that the mobility of components
430 through the reaction rims limits the rates of reaction. Concentration profiles through
431 the reaction rims shows that they are not homogenous in concentration and are not
432 well equilibrated. Diffusion through polycrystalline materials is most likely to be
433 concentrated along grain boundaries (Dohmen and Milke 2010).
434
435 *Dissolution / interface mechanism*
436 At high bulk water contents (8 wt.% H_2O in TSF8) the olivine-phlogopite interphase
437 boundary is completely open. Several textural features are observed at the olivine side
438 of the interphase region. These include an ASSL and a distorted olivine structure.
439 Similar features have been observed during the dissolution of olivine in the presence
440 of a fluid phase at completely different P-T conditions (90°C and 25 MPa) (Daval et
441 al 2013), suggesting that the mechanisms by which olivine dissolves are the same
442 over a wide range of P-T conditions. The same features are not observed in locations
443 where the interphase boundary had been mechanically opened during polishing and
444 quenching. Therefore the ASSL and distorted olivine must have formed at peak
445 conditions during the experiment. The formation of ASSL on the surfaces of silicates
446 has only been observed to form in the presence of a fluid phase. The fluid may only
447 consist of several monolayers (7-10 Å), giving it properties of a thin fluid film
448 (Hellmann et al, 2012).
449 The distorted region observed here and in Daval et al (2011) has not been
450 observed in other phases (Hellmann et al, 2012). From Table 3 it appears that the

451 distorted olivine region is not stoichiometric (Mg/Si <2) with a noticeable loss in Mg
452 relative to Si. This could be consistent with an exchange of Mg^{2+} with H^{+} by the
453 interaction with a fluid phase at peak experimental conditions (Pokrovsky and Schott,
454 2000; Daval et al., 2011). Protonation of μ_3-O sites causes an increase in the bond
455 lengths of adjacent atoms making them more labile (Liu et al, 2006). This leads to
456 breaking of Mg-O bonds and the release of Mg^{2+}, which becomes solvated as
457 $Mg^{2+}(H_2O)_6$. Silica is released more slowly than Mg and is the rate-limiting step in
458 dissolution. Although Si is in excess relative to Mg, the distorted region appears to
459 have less Si than in the non-distorted region (Figure 5b). This is because the distorted
460 region is less dense than the non-distorted region, i.e., both Mg and Si are being
461 removed during dissolution but Mg is being lost at a greater rate than Si, leading to
462 non-stoichiometry. This does not appear to be due to differences in the diffusion rates
463 of Mg and Si but is related to the strength of Mg-O (weaker) bonds relative to Si-O
464 bonds (stronger). The interaction of protons at the olivine interface and the loss of
465 both Mg and Si changes bond lengths and introduces both vacancies and defects into
466 the structure of the olivine. This results in the formation of distortions in the olivine
467 lattice that are observed by TEM. However the geometry of the distortions is difficult
468 to characterize.

469 The dissolution mechanism was not rate limiting. Rim forming components
470 must still pass through the reaction rim from the melt to the olivine-phlogopite
471 interface and we interpret rim growth in this sample (TSF8) to be limited by grain
472 boundary diffusion.

473

474 **Mass Balance**

During rim growth two reaction fronts are possible; one at the olivine – phlogopite interface and one at the phlogopite-melt interface. We calculate the mass balance distribution among phlogopite, forsterite and melt using the principals outlined in Ferry (1984) and extend these calculations by introducing some volume considerations.

In the Ca-free experiments, there are 6 system components (K_2O, Na_2O, Al_2O_3, SiO_2, MgO, H_2O) and 8 phase components (Mg_2SiO_4 – Forsterite, $KMg_3AlSi_3O_{10}(OH)_2$ – phlogopite, and the six oxides in the melt). Two (8-6) linearly independent net-transfer reactions describe mass transfer among olivine, phlogopite and melt during reaction.

(1) $K_2O + 6MgO + Al_2O_3 + 6SiO_2 + 2H_2O = 2KMg_3AlSi_3O_{10}(OH)_2$

(2) $2MgO + SiO_2 = Mg_2SiO_4$

The progress of reactions (1) and (2), referred to as $\xi 1$ and $\xi 2$ respectively, in each experiment are quantitatively recorded by the differences between the final melt composition and the hydrous starting glass.

(3) $MgO/Al_2O_3 = (n°MgO - 6\xi 1 - 2\xi 2)/(n°Al_2O_3 - \xi 1)$

(4) $SiO_2/Al_2O_3 = (n°SiO_2 - 6\xi 1 - \xi 2)/(n°Al_2O_3 - \xi 1)$

MgO/Al_2O_3 and SiO_2/Al_2O_3 are molar ratios in the melt after the experiment using TSF6 as an example, and $n°MgO$, $n°Al_2O_3$, and $n°SiO_2$ are the molar amounts of

MgO, Al_2O_3, and SiO_2 in hydrous melt at the start of the experiment (from Table 1, PHG3 glass) in units of mol/100 g minerals + melt, and $\xi 1$ and $\xi 2$ have units of mol/100 g. Substituting number values into equations 3 and 4 for all variables except ξ_1 and ξ_2,

(3') $0.108 = (0.048 - 6\xi 1 - 2\xi 2)/(0.187 - \xi 1)$

(4') $5.349 = (0.989 - 6\xi 1 - \xi 2)/(0.187 - \xi 1)$.

Therefore $\xi 1 = 0.01027$ $\xi 2 = -0.0165$ and $\xi 2/\xi 1 = -1.61$. This fits with what is observed in the experiments: phlogopite crystallizes and forsterite dissolves. The total amount of phlogopite formed in the experiment is ξ_1. We must now calculate the amount of phlogopite in the rims relative to phlogopite formed as a liquidus phase in the melt. The amount of phlogopite formed in the melt is determined by image analysis of BSE images using the ImageJ software. By producing a binary color image, the % area of phlogopite and melt can be measured. We find that in sample TSF6 the melt contains approximately 3.65 % phlogopite by volume. Using the known weighed amounts of solid material (forsterite + glass) in the sample and the density of olivine (3.22 g/cm^3) and melt (2.38 g/cm^3 – using the method in McBirney, 1993) the volume proportion of both phases at the start of the experiment can be calculated (forsterite = 11% and melt = 89%). The amount of phlogopite in the melt as a percentage of the total sample is approximately 3.25 %. An estimated volume of each olivine grain is calculated using a diameter of 375 μm (median of size range 250-500 μm of crushed forsterite) and spherical shapes. By deducting the volume of olivine after the experiments (375 – 2*rim thickness), the volume of rim phlogopite

525 can be estimated (0.92% of total sample). The percentage of phlogopite in the rims
526 out of the total amount of phlogopite formed is therefore 22%. By multiplying the
527 ratio of $\xi 2/\xi 1$ by 0.22 (=-0.35) we can obtain an overall equation of the reaction of
528 forsterite to phlogopite;
529
530 (5). $0.35\ Fo + K_2O + 5.3\ MgO + Al_2O_3 + 2.65\ SiO_2 + 2H_2O = 2\ Phlog$
531
532
533 Reaction (5) is the sum of the two reactions, one at the olivine-phlogopite
534 interface and the other at the phlogopite-melt interface. Considering the large fraction
535 of MgO needed to form phlogopite after (5) and its low concentration in the melt
536 (Table 1), the availability of MgO seems to limit phlogopite formation.
537 Simple volumetric considerations can be used to reconstruct the position of the
538 original olivine-melt interface and the respective contributions of the two partial
539 reactions. This reconstruction makes use of the basic assumption that once an olivine
540 grain is encased in a phlogopite mantle, any further mica formation at the inner
541 (olivine-phlogopite) interface is spatially restricted to the volume made available by
542 olivine dissolution. As reaction rim formation is controlled by grain-boundary
543 diffusion, the outward diffusion of excess components from the olivine (e.g. Mg)
544 should be expected to be similarly effective as the inward diffusion (e.g. of Al and K)
545 from the melt.
546 The molar volumes of forsterite (2 MgO p.f.u.) and phlogopite (3 MgO p.f.u.)
547 are 44 and 150 cm^3mol^{-1}, respectively. Dissolution of 1 mol forsterite thus releases
548 enough MgO for precipitation of 0.67 mol phlogopite, i.e. 44 vol% phlogopite could
549 form by replacement of forsterite at the olivine-phlogopite interface whereas 56 vol%

must crystallize outwardly as an overgrowth fed by MgO diffusion through the rim. Combining these volume constraints in the reaction rims and the volumetric fraction of rim vs. bulk phlogopite we can now write weighed reactions for all three contributions to phlogopite formation in the experiments that sum up to reaction (5):

(5a). $0.35\ Fo + 0.05\ K_2O + 0.05\ Al_2O_3 + 0.15\ SiO_2 + 0.11\ H_2O = 0.11\ Phlog + 0.4\ MgO$

(5b). $0.07\ K_2O + 0.4\ MgO + 0.07\ Al_2O_3 + 0.2\ SiO_2 + 0.13\ H_2O = 0.13\ Phlog$

(5c). $0.88\ K_2O + 5.3\ MgO + 0.88\ Al_2O_3 + 2.3\ SiO_2 + 1.76\ H_2O = 1.76\ Phlog$

where (5a) applies to the forsterite-phlogopite interface, (5b) to the phlogopite-melt interface, and (5c) to the bulk phonolite. This mass-and-volume balance explains several observations from the experiments.

Firstly, the dominance of (5c) over reactions (5a+b) indicates why the MgO concentration in the quenched glass after experiment was lower than the in the initial glass although a source of MgO was added to this glass. The olivine-mica core-rim-structures are essentially neutral with respect to the MgO balance because all released MgO can immediately be incorporated into rim phlogopite.

Secondly, in the rims a maximum of 44 vol% of phlogopite can be formed at the forsterite-phlogopite interface, such that the initial forsterite-melt contact must be located inside the phlogopite rims and nearer to the forsterite than to the melt interface. The 44 vol% is an upper boundary because the phlogopite in contact with melt could have acted as a substrate for further phlogopite overgrowths fed by MgO

575 from the melt. From this perspective the transition in chemical composition for all
576 major components in phlogopite (K_2O, MgO, Al_2O_3, SiO_2) (Figure 8) can be
577 explained in terms of growth directions. The rather flat part of the concentration
578 profile (apart from mixed analyses at the olivine-phlogopite interface) in the inner
579 parts of the rims is interpreted as crystallization at the olivine-phlogopite interface
580 buffered to local equilibrium, whereas the outwards increasingly scattered element
581 distribution represents crystallization at the phlogopite-melt interface. The transition
582 between these zones that might represent the original forsterite-melt contact is located
583 at about one third rim thickness from the olivine-phlogopite interface in accordance
584 with the mass-volume balancing.

585 Finally, the balancing provides solid estimates for mass fluxes through the
586 phlogopite rims. The chemical fluxes are mutually interrelated by crystal volume and
587 ionic charges, and in such complex reactions it seems improbable that one single
588 component controls the distribution of all the others and acts as being rate-limiting.
589 However, the outward flux of the MgO component from the forsterite to the melt
590 interface is clearly the largest flux involved and might play a leading role for overall
591 rim growth rates.

592

593 **Effects of H_2O on grain boundary diffusion**

594 The experimental data in this study shows two clear observations; (a) growth of
595 phlogopite rims is rate limited by diffusion along phlogopite-phlogopite grain
596 boundaries and (b) rim growth rates increase with increasing bulk water contents of
597 the sample charge (see Figure 2c). It therefore appears that the diffusion rates of
598 chemical components along the grain boundaries are increased when the water
599 content of the melt is increased. As hydrous species (H^+, OH^-) will be exchanged

between grain boundaries and the melt, the amounts of atomically bound fluid along grain boundaries are expected to increase as the water content of the melt increases. Atomically bound fluid species will lower the activation energies required for diffusion by introducing higher concentrations of weaker hydrogen bounds relative to Si-O or M-O (where M = a metal cation) bonds that are dominant in dry grain boundaries (Rubie, 1986). Increasing amounts of atomically bound fluid species along grain boundaries have been shown in many other systems to increase rates of diffusion and thereby increase rim growth rates (Liu et al, 1997; Yund, 1997; Keller et al, 2008; Carlson, 2010; Gardés et al, 2012). Our data (Figure 2c) are consistent with such an interpretation. The phlogopite-phlogopite grain boundaries formed in the reaction rims in our experiments are partially hydrated by atomically bound fluid species. Increasing amounts of H_2O in the melt results in further hydration of the grain boundaries leading to faster diffusion rates and rim growth.

Our results demonstrate the effects of increasing melt water contents will have on the rates and progress of metasomatic reactions in the upper mantle. The amount of water contained within hydrous grain boundaries, even if only at very low amounts (ppm) may significantly enhance the mobilities and exchange of elements between the metasomatic melt and the wall rock.

Origin of pores and open grain/ inter-phase boundaries.

Pores and open grain and interphase boundaries were observed in the TEM foils of samples with low water (e.g. TSF2) and high water (e.g. TSF8). These either formed during quenching (cooling and unloading of pressure) or by the presence of an intergranular fluid at peak experimental conditions. If a free fluid formed at these pressures and temperatures it should contain a significant amount of dissolved solute

625 species (Manning, 2004). During quenching a fluid should therefore form precipitates
626 observable under TEM.

627 During cooling and unloading of pressure all phases will change in volume.
628 The melt, which is the most voluminous phase in each sample, will contract (see
629 Seifert et al., 2013). This has caused some large cracks to appear across the samples
630 that cross cut other features (some are observable in Figure. 1b.). Additionally,
631 polishing weakens the phlogopite leading to wedge shaped voids in the surface
632 (extending <30 nm into the sample) that are observable in the TEM foils (see Figure
633 3a). The phlogopite in the reaction rims will also experience a net decrease in volume
634 due to greater amounts of contraction during cooling compared to expansion during
635 unloading of pressure (Tutti et al, 2000; Comodi et al, 2004), and this could cause
636 some grain boundaries to open. Furthermore, contraction of the surrounding melt and
637 or olivine may also result in stress on the reaction rims leading to partial opening of
638 the grain and interphase boundaries. Opening of grain boundaries by anisotropic
639 thermal contraction has also been observed in quartz for example (Kruhl et al., 2013).
640 This provides a sound explanation for the formation of most of the open grain
641 boundaries observed (for example those in Figure 3a.) that do not contain any
642 evidence of material precipitated from a fluid phase. Furthermore it is also possible
643 that that the volatile-rich phase within the grain boundaries exsolves a fluid phase
644 during quenching. This could be a possible explanation for the origin of micro-pores
645 along grain boundaries (Figure 3b).

646 Pore cavities along grain boundaries in sample TSF8 (Figure 3d) have
647 negative phlogopite crystal shapes. We suggest that it is unlikely that such textures
648 would form under rapid quenching. As a comparison, the pores along the grain
649 boundaries in sample TSF2 Figure 3b are distinctly more rounded or have irregular

650 shapes. Therefore the pores in sample TSF2 are likely to have formed during
651 quenching whereas those in sample TSF8 appear to have formed at peak conditions.
652 However, fluid pores at peak P-T conditions are likely to be transient and dynamic
653 (Billa et al., 2013; Norberg et al., 2013), due to simultaneous dissolution and
654 precipitation at the interfaces between the pore fluid and surrounding phlogopite.

655 The open interphase boundary in sample TSF8 contains an ASSL and
656 dissolution features in olivine (Figure 5) that have been observed previously in
657 samples where a fluid has reacted with olivine (Daval et al., 2011) and other phases
658 (Hellmann et al., 2012). This is strong evidence to support the idea that a free fluid
659 was present at peak experimental conditions and reacted with the olivine surface.
660 Although it cannot be conclusively proven, we interpret these results as evidence of a
661 fluid phase at the interphase boundary in sample TSF8 at peak experimental
662 conditions.

663 In sample TSF2 a small open cavity containing amorphous material is present
664 at the olivine-phlogopite interphase boundary. The amorphous material is enriched in
665 Si and Al implying transport of Al from the melt to the olivine interface. This feature
666 is likely to have existed at peak conditions either as a single solute rich fluid phase
667 (which separated during quenching) or an unmixed melt + fluid phase.

668 Although many open grain boundary and pore features observed in TEM are
669 most likely to have formed by contraction of the sample during cooling, there do
670 appear to be evidence of some fluid being present at peak experimental conditions and
671 that the amount of fluid appears to be greater in samples with greater amounts of
672 water in the melt. We suggest that the formation of a fluid phase is a distinct
673 possibility but this cannot be equivocally proved from our data as the rims cannot be
674 viewed during peak conditions. Any formation of a fluid phase along grain boundaries

or at interphase boundaries would be a particularly surprising result considering that the melt is undersaturated with fluid.

Crystallization of phlogopite will increase the amount of H_2O in the melt (recalling that phlogopite contains less water than the starting melt). For example, in sample TSF8, however, it is unlikely that the crystallization of matrix phlogopite was enough to saturate the melt in H_2O. Experiments using PHG2 and up to 12.4 wt.% H_2O have been conducted but they did not become saturated with H_2O (unpublished data). A satisfactory explanation as to why small amounts of free fluid might form in the grain and interphase boundaries during reaction rim growth is lacking. The properties of hydrated grain boundaries at upper mantle conditions and the exchange of fluid species with silicate melts is poorly understood. We can speculate that from our results it may be possible to form small localized amounts of fluid under non-equilibrium conditions but further work is necessary to understand this phenomena and its implications for mantle metasomatism.

APPLICATIONS

Residence times

Reaction rims can be used to provide estimates of residence times of phenocrysts or xenocrysts in their host magma (Rutherford, 2008). Specifically, the reaction rates calculated here can be used to estimate residence times of olivine xenocrysts in the Heldburg Phonolite (Grant et al, 2013). The natural phlogopite rim thicknesses are typically around 20-30 μm. In Figure 2c a parabolic rate law (R) was calculated for each experiment at the same P-T conditions but varying H_2O. As R = m^2/s, it is simple to rearrange this and calculate a residence time (s) from a known rim thickness

in nature (~25 μm) and known R at different melt H_2O conditions (at 950°C and 1.0 GPa).

This gives a rough estimate of the residence times at different conditions (Figure 9). At the highest bulk H_2O the estimated residence time would be around several hours, whereas at the lowest bulk H_2O the estimated residence times would be up to around 100 days. It is more likely that the water content in the melt at Heldburg was towards the lower end of this scale averaging at about 4 wt.% (although it varies between 3-6 wt.%). This was estimated using calculations (from Ridolfi and Renzulli, 2012), from amphibole compositions in Grant et al. (2013). Temperatures of the Heldburg Phonolite during reaction rim formation are estimated to be between 850-950ºC (Grant et al, 2013). This should therefore give residence times of several weeks to a few months for the natural reaction rims. This data is consistent with previous estimates given within Grant et al (2013).

Two experiments at 1000°C are also shown in Figure 9, to demonstrate the effects of temperature on estimated residence times. It is clear that the water content of the melt will have an important effect, as well as temperature, on the rim growth rates and constraining both parameters will be important if reaction rims of this kind are to be used as a way of calculating residence times. It is also potentially possible to calculate the melt water contents based on H_2O partitioning between clinopyroxene and melt (Wade et al, 2008; O'Leary et al, 2010), although data for phonolite melts are lacking. In systems where the rim growth was rate limited by diffusion in the melt, these results may still apply. If convection or any kind of mechanical movement of xenocryst relative to the melt takes place, and this is highly likely during eruption, then melt boundary layers could be eroded. This means that diffusion through the rim itself will have a more direct effect on rim growth rates in a dynamic system rather

725 than a static experimental setting.

726

727

728 **ACKNOWLEDGEMENTS**

729 The authors would like to thank the German Research Foundation (DFG) for the FOR
730 funding for this project (MI1205/2-2). We thank Anja Schreiber for FIB sample
731 preparation, Katharina Marquardt, Luiz Morales and Wilhelm Heinrich for helpful
732 discussions.

733

734 **BIBLIOGRAPHY**

735 Aoki, K. (1975) Origin of phlogopite and potassic richterite bearing peridotite
736 xenoliths from South Africa. Contributions to Mineralogy and Petrology, 53, 145-
737 156.

738 Arai, S., and Takahashi, N. (1989) Formation and compositional variation of
739 phlogopites in the Horoman peridotite complex, Hokkaido, northern Japan:
740 implications for origin and fractionation of metasomatic fluids in the upper mantle.
741 Contributions to Mineralogy and Petrology, 101, 165-175.

742 Arima, M., and Edgar, A.D. (1983) High pressure experimental studies on a katunigte
743 and their bearing on the genesis of some potassium-rich magmas of the west branch
744 of the African rift. Journal of Petrology, 24, 166-187.

745 Billa, M.A., Timms, N.E., Toy, V.A., Hart, R.D., and Prior, D.J. (2013) Grain
746 boundary dissolution porosity in quartzfeldspathic ultramylonites: implications for
747 permeability enhancement and weakening of mid-crustal shear zones. Journal of
748 Structural Geology, 53, 2-14.

749 Bodinier, J-L., Menzies, M.A., Shimizu, N., Frey, F.A., and McPherson, E. (2004)

Silicate, hydrous and carbonate metasomatism at Lherz, France: contemporaneous derivatives of silicate melt-harzburgite reaction. Journal of Petrology, 45, 299-320.

Carlson, W.D. (2010) Dependence of reaction kinetics on H_2O activity as inferred from rates of intergranular diffusion of aluminum. Journal of Metamorphic Geology, 28, 735-752.

Carmichael, I.S.E. (1967) The mineralogy and petrology of the volcanic rocks from the Leucite Hills, Wyoming. Contributions to Mineralogy and Petrology, 15, 24-66.

Carroll, M.R., and Blank, J.G. (1997) The solubility of H_2O in phonolite melts. American Mineralogist, 82, 549-556.

Çoban, H., and Flower, M.F.J. (2006) Mineral phase compositionsin silica-undersaturated 'leucite' lamproites from the Bucak area, Isparta, SW Turkey. Lithos, 89, 275-299.

Comodi, P., Fumagalli, P., Montagnoli, M., and Zanazzi, P.F. (2004) A single-crystal study on the pressure behavior of phlogopite and petrological implications. American Mineralogist, 89, 647-653.

Coombs, M.L., and Gardner, J.E. (2004) Reaction rim growth on olivine in silicic melts: implications for magma mixing. American Mineralogist, 89, 748-758.

Daval, D., Sissman, O., Menguy, N., Saldi, G., Guyot, F., Martinez, I., Corvisier, J., Garcia, B., Machouk, I., Knauss, K.G., and Hellmann, R. (2011) Influence of amorphous silica layer formation on the dissolution rate of olivine at 90°C and elevated pCO_2. Chemical Geology, 284, 193-209.

Daval, D., Hellmann, R., Saldi, G.D., Wirth, R., and Knauss, K.G. (2013) Linking nm-scale measurements of the anisotropy of silicate surface reactivity to macroscopic dissolution rate laws: new insights based on diopside. Geochimica et Cosmochimica Acta, 107, 121-134.

775 Davis, L.L., and Smith, D. (1993) Ni-rich olivine in minettes from Two Buttes,
776 Colorado: a connection between potassic melts from the mantle and low Ni partition
777 coefficients. Geochimica et Cosmochimica Acta, 57, 123-129.
778 Dohmen, R., and Chakraborty, S. (2003) Mechanism and kinetics of element and
779 isotopic exchange mediated by a fluid phase. American Mineralogist, 88, 1251-1270.
780 Dohmen, R., and Milke, R. (2010) Diffusion in polycrystalline materials: grain
781 boundaries, mathematical models and experimental data. Reviews in Mineralogy and
782 Geochemistry, 72, 921-970.
783 Draper, D.S., and Green, T.H. (1997) P-T phase relations of silicic, alkaline,
784 aluminous mantle-xenolith glasses under anhydrous and C-O-H fluid saturated
785 conditions. Journal of Petrology, 38, 1187-1224
786 Ferry, J.M. (1984) Phase composition as a measure of reaction progress and an
787 experimental model for the high-temperature metamorphism of mafic igneous rocks.
788 American Mineralogist, 69, 677-691.
789 Foley, S. (1992) Vein-plus-wall-rock melting mechanisms in the lithosphere and the
790 origin of potassic alkaline magmas. Lithos, 28, 435-453.
791 Foley, S.F., Andronikov, A.V., and Melzer, S. (2002) Petrology of ultramafic
792 lamprophyres from the Beaker Lake area of Eastern Antarctica and their relation to
793 the breakup of Gondwanaland. Mineralogy and Petrology, 74, 361-384.
794 Gardés, E., Wunder, B., Marquardt, K., and Heinrich, W. (2012) The effect of water
795 on intergranular mass transport: new insights from diffusion-controlled reaction rims
796 in the MgO-SiO2 system. Contributions to Mineralogy and Petrology, 164, 1-16.
797 Grant, T.B., Milke, R., Pandey, S., and Jahnke, H. (2013) The Heldburg Phonolite,
798 Central Germany: reactions between phonolite and xenocrysts from the upper mantle
799 and lower crust. Lithos, 182-183, 86-101.

Grieco, G., Ferrario, A., Von Quadt, A., Koeppel, V., and Mathez, E.A. (2001) The zircon-bearing chromitites of the phlogopite peridotite of FInero (Ivrea Zone, Southern Alps): evidence and geochronology of a metasomatized mantle slab. Journal of Petrology, 42, 89-101.

Harlov, D.E., and Milke, R. (2002) Stability of corundum + quartz relative to kyanite and sillimanite at high temperature and pressure. American Mineralogist, 87, 424-432.

Hellmann, R., Wirth, R., Daval, D., Barnes, J-P., Penisson, J-M., Tisserand, D., Epicier, T., and Hervig, R.L. (2012) Unifying natural and laboratory chemical weathering with interfacial dissolution-reprecipitation: a study based on the nanometer-scale chemistry of fluid-silicate interfaces. Chemical Geology, 294-295, 203-216.

Henderson, C.M.B., Richardson, F.R., and Charnock, J.M. (2012) The Highwood Mountains potassic igneous province, Montana: mineral fractionation trends and magmatic processes revisited. Mineralogical Magazine, 76, 1005-1051.

Johannes, W. (1973) Eine vereinfachte Piston-Zylinder-Apparatur hoher Genauigkeit. Neues Jahrbuch Für Mineralogie 337-351.

Johannes, W., Bell, P.M., Mao, H.K., Boettcher, A.L., Chipman, D.W., Hays, J.F., Newton, R.C., and Seifert F. (1971) An interlaboratory comparison of piston-cylinder pressure calibration using the albite-breakdown reaction. Contributions to Mineralogy and Petrology, 32, 24-38.

Keller, L.M., Wunder, B., Rhede, D., and Wirth, R. (2008) Component mobility at 900°C and 18 kbar from experimentally grown coronas in a natural gabbro. Geochimica et Cosmochimica Acta, 72, 4307-4322.

Kruhl, J. H., Wirth, R., and Morales, L. F. (2013). Quartz grain boundaries as fluid

825 pathways in metamorphic rocks. Journal of Geophysical Research, 118, 5, 1957-1967
826 Liu, M., Peterson, J.C., and Yund, R.A. (1997) Diffusion-controlled growth of albite
827 and pyroxene reactions rims. Contributions to Mineralogy and Petrology,126, 217-
828 223.
829 Liu, Y., Olsen, A.A., Rimstidt, J.D. (2006) Mechanism for the dissolution of olivine
830 series minerals in acidic solutions. American Mineralogist, 91, 455-458.
831 Lloyd, F.E., Edgar, A.D., Forsyth, D.M., and Barnett, R.L. (1991) The paragenesis of
832 upper-mantle xenoliths from the Quaternary volcanics south-east of Gees, West Eifel,
833 Germany. Mineralogical Magazine, 55, 95-112.
834 Lloyd, F.E., Woolley, A.R., Stoppa, F., and Eby, G.N. (2002) Phlogopite-biotite
835 parageneses from the K-mafic-carbonatite effusive magmatic association of Katwe-
836 Kikorongo, SW Uganda. Mineralogy and Petrology, 74, 299-322.
837 Luth, W.C: (1967) Studies in the system $KAlSiO_4$-Mg_2SiO_4-SiO_2-H_2O: inferred phase
838 relations and petrologic application. Journal of Petrology, 8, 372-416.
839 Manning, C.E. (2004) The chemistry of subduction-zone fluids. Earth and Planetary
840 Science Letters, 223, 1-16.
841 McBirney, A. R. (1993). Igneous petrology, 463. p. Jones & Bartlett Learning.
842 Milke, R., Neusser, G., Kolzer, K., and Wunder, B. (2013) Very little water is
843 necessary to make a dry solid silicate system wet. Geology, 41, 247-250.
844 Neal, C.R., and Taylor, L. A. (1989) The petrography and composition of phlogopite
845 micas from the Blue Ball Kimberlite, Arkansas: a record of chemical evolution during
846 crystallization. Mineralogy and Petrology, 40, 207-224.
847 Norberg, N., Harlov, D., Neusser, G., Wirth, R., Rhede, D., and Morales, L. (2013)
848 Experimental development of patch perthite from synthetic cryptoperthite:
849 microstructural evolution and chemical re-equilibration. American Mineralogist, 98,

1429-1441.

O'Leary, J.A., Gaetani, G.A., and Hauri, E.H. (2010) The effect of tetrahedral Al^{3+} on the partitioning of water between clinopyroxene and silicate melt. Earth and Planetary Science Letters, 297, 111-120.

Pilet, S., Baker, M.B., Müntener, O., and Stolper, E.N. (2011) Monte Carlos simulations of metasomatic enrichment in the lithosphere and implications for the source of alkaline basalts. Journal of Petrology, 52, 1415-1442.

Pokrovsky, O.S. and Schott, J. (2000) Kinetics and mechanism of forsterite dissolution at 25ºC and pH from 1 to 12. Geochemica et Cosmochimica Acta, 64, 3313-3325.

Prouteau, G., Scaillet, B., Pichavant, M., and Maury, R. (2001) Evidence for mantle metasomatism by hydrous silicic melts derived from subducted oceanic crust. Nature, 410, 197-200.

Ridolfi, F. and Renzulli, A. (2012). Calcic amphiboles in calc-alkaline and alkaline magmas: thermobarometric and chemometric empirical equations valid up to 1,130ºC and 2.2 GPa. Contributions to Mineralogy and Petrology, 163, 877-895.

Rubie, D.C. (1986) The catalysis of mineral reactions by water and restrictions on the presence of aqueous fluid during metamorphism. Mineralogical Magazine, 50, 399-415.

Rutherford, M.J. (2008) Magma ascent rates. Reviews in Mineralogy and Geochemistry, 69, 241-271.

Schilling, F., and Wunder, B. (2004) Temperature distribution in piston-cylinder assemblies: numerical simulations and laboratory experiments. European Journal of Mineralogy, 16, 7-14.

Schmidt, B.C., and Behrens, H. (2008) Water solubility in phonolite melts: influence

of melt composition and temperature. Chemical Geology, 256, 259-268.

Seifert, F., & Schreyer, W. (1971) Synthesis and stability of micas in the system K_2O -MgO-SiO_2-H_2O and their relations to phlogopite. Contributions to Mineralogy and Petrology, 30, 196-215.

Seifert, R., Malfait, W.J., Petitgirard, S. and Sanchez-Valle, S. (2013) Density o phonolitic magmas and time scales of crystal fractionation in magma chambers. Earth and Planetary Science Letters, 381, 12-20.

Semiz, B., Çoban, H., Roden, M.F., Özpinar, Y., Flower, M.F.J., and McGregor, H. (2012) Mineral composition in cognate inclusions in late Miocene-early Pliocene potassic lamprophyres with affinities to lamproites from the Denizili region, Western Anatolia, Turkey: implications for uppermost mantle processes in a back arc setting. Lithos, 134-135, 253-272.

Stiefenhofer, J., Viljoen, K.S., and Marsh, J.S. (1997) Petrology and geochemistry of peridotite xenoliths from the Letlhakane kimberlites, Botswana. Contributions to Mineralogy and Petrology, 127,147-158.

Sudo, A., and Tatsumi, Y. (1990) Phlogopite and K-amphibole in the upper mantle: implication for magma genesis at subduction zones. Geophysical research letters, 17, 29-32.

Thibault, Y., Edgar, A.D., and Lloyd, F.E. (1992) Experimental investigation of melts from a carbonated phlogopite lherzolite: implications for metasomatism in the continental lithospheric mantle. American Mineralogist, 77, 784-794.

Trønnes, R. G. (2002) Stability range and decomposition of potassic richterite and phlogopite end members at 5-15 GPa. Mineralogy and Petrology, 74, 129-148.

Tutti, F., Dubrovinsky, L.S., and Nygren, M. (2000) High-temperature study and thermal expansion of phlogopite. Physics and Chemistry of Minerals, 27, 599-603.

Wade, J.A., Plank, T., Hauri, E.H., Kelley, K.A., Roggensack, K., and Zimmer, M. (2008) Prediction of magmatic water contents via measurement of H_2O in clinopyroxene phenocrysts. Geology, 36, 799-802.

Wirth, R. (2004) Focused Ion Beam (FIB): a novel technology for advanced application of micro- and nanoanalysis in geosciences and applied mineralogy. European Journal of Mineralogy, 16, 863-876.

Wulff-Pedersen, E., Neumann, E-R., and Jensen, B.B. (1996) The upper mantle under La Palma, Canary Islands: formation of Si-K-Na-rich melt and its importance as a metasomatic agent. Contributions to Mineralogy and Petrology, 125, 113-139.

Wunder, B., and Melzer, S. (2003) Experimental evidence on phlogopitic mantle metasomatism induced by phengite dehydration. European Journal of Mineralogy, 15, 641-647.

Yund, R. (1997) Rates of grain boundary diffusion through enstatite and forsterite reaction rims. Contributions to Mineralogy and Petrology, 126, 224-236.

Zanetti, A., Mazzucchelli, M., Rivalenti, G., and Vannucci, R. (1999) The Finero phlogopite-peridotite massif: an example of subduction-related metasomatism. Contributions to Mineralogy and Petrology, 134, 107-122.

Zhang, Y., Ni, H., and Chen, Y. (2010) Diffusion in silicate melts. Reviews in Mineralogy and Geochemistry, 72, 311-408

Tables

Table 1. Starting material compositions. No data is given for the synthetic olivine as it is pure forsterite.

925 Table 2. Experimental run conditions, including measured rim thicknesses. All time
926 series experiments use Ca-free glass (PHG3), and all "Single experiments" use Ca-
927 bearing glass (PHG2).
928
929 Table 3. EDX analyses of distorted and undistorted olivine regions in sample TSF8.
930 Error for Mg analyses are ~8% and the error for Si analyses are~5% and the
931 calculated error for each analysis is given in brackets. For Si/Mg the calculated error
932 propagation is given the brackets.
933
934 Table 4. Phlogopite compositions. X (in μm) refers to the distance along the rim line
935 scan shown in Figure 8, where X=0 is the olivine interface and X>0 is the distance
936 from the olivine interface. Errors in brackets are to 2 decimal places.
937
938 Figures
939 Figure 1. Back scattered electron (BSE) images of natural and experimental reaction
940 rims. Panel a – image of a natural examples of a phlogopite reaction (with minor
941 diopside) on a olivine xenocryst. Amounts of diopside vary (see Grant et al, 2013 for
942 further examples) Panel b – image taken of SC31 showing double rims of phlogopite
943 + diopside. Diopside is also a liquidus phase in this experiment. Note the interstitial
944 glass and discontinuous thickness of the diopside outer rim. Inner phlogopite rim
945 thicknesses are fairly consistent. Convoluted olivine – phlogopite interphases are
946 clearly observable. Note large unfilled cracks that crosscut all other features. Panel c –
947 image from TSF6 demonstrating that single rims of phlogopite form in Ca-free melt.
948 Phlogopite is also an abundant liquidus phase.
949

Figure 2. Rim growth with time and melt water content. Panel a-b shows the variation in rim thickness with time for the time series experiments (Ca-free melt). The ranges in bulk water content are given for each set of time series experiments. Error bars are the standard deviation of rim thickness for each experiment. Panel c shows the increase in rim growth with bulk water content of the sample at 950°C. Black squares are the time series experiments and the grey circles are single experiments with Ca-bearing melt. Error bars for the bulk water content corresponds to the likely maximum variations in the amount of olivine from 10-20% of the bulk in the sample.

Figure 3. HAADF, TEM bright field and HREM images of phlogopite-phlogopite grain boundaries. The images only contain phlogopite. Images a-c are from sample TSF2 and d-e TSF8. Areas marked by an A are pores cavities, and areas marked by a B are open grain boundaries. a) HAADF image: a pore along a grain boundary, B = open grain boundary. Panel b is a higher magnification of the HAADF image of the grain boundary with the highlighted pore in panel a. Panel c is a HREM lattice fringe image of a phlogopite-phlogopite grain boundary. The dashed white line shows the location of the phlogopite-phlogopite grain boundary. The lattice fringes are touching. Panel d is a TEM bright-field image showing a grain boundary decorated by isolated pores typically around 100 nm in size. Panel e is a TEM bright-field image showing a grain boundary decorated by small (<20 nm) pores that are very closely spaced.

Figure 4. TEM images of olivine – phlogopite interphase boundaries. A and B have the same meanings as in Figure 3 and dashed lines indicate the location of the interphase boundary. Panel a, a HREM lattice fringe image is taken from sample TSF6 and shows a closed interphase boundary where the lattice fringes of phlogopite

975 and olivine are touching. Panel b, a HAADF image, is from sample TSF2 and shows a
976 micro-pore at the olivine interface. Facets in the olivine surface are visible at these
977 resolutions. Panel c (HAADF image) is from sample TSF8 and shows a completely
978 open grain boundary between olivine and phlogopite. The image is around 4.5μm
979 across. Black square shows the location of the images taken by HRTEM in Figure 5.
980 Panel d (HAADF image) shows a higher magnification image of the open grain
981 boundary that tapers out and closes towards the top left of the image.
982
983 Figure 5. HRTEM imaging of the interface region shown in panel c in Figure 4 from
984 sample TSF 8. The analyses are of the interface region and olivine only. The Si-jump
985 ratio grey-scale map in panel a with light grey indicating high Si and dark grey lower
986 Si. An intensity line scan in panel b shows four main regions across the interface,
987 denoted by numbers 1-4 in each panel. The y-axis on this plot is in arbitrary units that
988 relate to the amount of Si detected in the jump ratio image. 1 corresponds to the
989 interface region, 2 is a thin 8-10 nm amorphous Si-rich surface layer (ASSL) similar
990 to those observed by Hellmann et al (2012), 3 is a distorted olivine and shows a
991 mottled texture in panel d, and region 4 is non-distorted olivine. The y-axis in panel b
992 is in arbitrary units. Panel C shows the FFT diffraction spots of the distorted olivine,
993 Panel D shows the FFT diffraction spots for the non-distorted olivine. Panel e is a
994 HREM image of the non-distorted olivine and Panel f shows the layer sequence of the
995 interface region, ASSL and distorted olivine.
996
997 Figure 6. HRTEM and HAADF images of melt pockets. Both images are form sample
998 TSF2. The right hand panel image is about 1.25μm wide. Note the partially open
999 grain boundaries. In the HREM image in panel a the non-crystalline material is

1000 characterized by the absence of lattice fringes as seen in olivine and phlogopite. This
1001 amorphous material is located adjacent to an open cavity (marked with an A). A and
1002 B labels are the same as in Figure 3 and 4, however the pore cavity in Figure 6a
1003 (labeled with an A) appears different here to those in Figures 3 and 4 because under
1004 HRTEM the back wall of the cavity is partially visible. C = amorphous material.
1005 When analyzed the amorphous material was very Si and Al rich with very small
1006 amounts of K and Mg.
1007
1008 Figure 7. Line scans taken in samples TSF4 (black circles) and TSF6 (grey circles)
1009 using the FEG probe at the GFZ Potsdam. All line scans go from the olivine, through
1010 the phlogopite reaction rim and extend through the glass. Dashed lines separate
1011 olivine, phlogopite rims and glass in sequential order going from left to right in each
1012 panel. Error bars correspond to the standard deviation from the FEG-probe data. See
1013 the analytical methods section for how this data was collected.
1014
1015 Figure 8. Line scans through phlogopite reaction rims from SC33.
1016
1017 Figure 9. Using the calculated rim growth rates from each experiment the predicted
1018 time to produce a rim with a thickness of 25 μm is estimated. This equates to an
1019 estimate residence time of the olivine xenocrysts found within the Heldburg Phonolite
1020 (Grant et al, 2013) that have rim thicknesses that are typically <100 μm. Grey circles
1021 are for experiments at 950ºC and black circles for two experiments at 1000ºC.

Table 1. Starting materials

	PHG2 glass (N=13)	PHG3 weighed	PHG3 glass (N=28)	San Carlos olivine (N=40)
SiO_2	60.50 (0.31)	61.46	60.09 (0.67)	39.43 (0.30)
TiO_2	-	-	-	-
Cr_2O_3	-	-	-	-
Al_2O_3	19.39 (0.27)	19.69	19.57 (0.60)	0.04 (0.02)
FeOtot	-	-	-	8.47 (0.19)
NiO	-	-	-	0.38 (0.02)
MgO	1.95 (0.06)	1.99	1.98 (0.05)	52.07 (0.30)
CaO	2.51 (0.03)	-	-	0.11 (0.01)
Na_2O	8.43 (0.18)	7.95	6.84 (0.29)	-
K_2O	7.12 (0.08)	8.9	8.67 (0.08)	-
Total	99.94	99.99	97.18	100.55

Table 2. Experimental run conditions

Sample	Olivine type	Temperature (ºC)	Pressure (Kbar)	Bulk water (H_2O wt.%)	Melt water	Duration (hrs)	Rim thickness (µm)
Time series							
TSF2	Forsterite	950	10.7	6.5	7.7	168.0	21.3 (3.9)
TSF3	Forsterite	950	10.7	5.6	6.7	74.0	13.8 (3.5)
TSF4	Forsterite	950	10.7	5.7	6.8	3.0	1.7 (1.5)
TSF6	Forsterite	950	10.7	5.7	6.8	26.0	7.9 (3.4)
TSF7	Forsterite	950	10.7	3.9	4.6	26.0	2.8 (1.1)
TSF11	Forsterite	950	10.7	4.2	5.0	72.5	5.3 (2.2)
TSF14	Forsterite	950	10.7	4.2	5.0	5.3	1.6 (0.5)
TSF8	Forsterite	950	10.7	7.2	8.6	26.0	25.0 (4.2)
TSF12	Forsterite	950	10.7	8.0	9.5	72.5	34.0 (5.4)
TSF13	Forsterite	950	10.7	7.8	9.3	5.3	11.8 (2.8)
Single experiments							
Fo25	Forsterite	950	14.7	9.1	10.6	3.0	14.1 (1.5)
Fo28	Forsterite	950	10.7	8.6	10.0	3.0	10.7 (1.5)
Fo30	Forsterite	950	10.7	7.7	9.0	3.0	10.2 (2.0)
SC31	San Carlos	1000	14.7	4.2	4.9	3.8	8.5 (1.3)
Fo32	Forsterite	1000	14.7	4.7	5.5	3.8	6.8 (1.1)
SC33	San Carlos	950	10.7	3.8	4.4	24.0	6.6 (1.4)

Table 3.

Point no.	Mg	Si	Mg / Si	Location
1	63.5 (5.1)	36.5 (1.8)	1.74 (0.09)	distorted
2	66.4 (5.3)	33.6 (1.7)	1.98 (0.09)	undistorted
3	61.4 (4.9)	38.6 (4.9)	1.59 (0.09)	distorted
4	66.6 (5.3)	33.4 (1.7)	1.99 (0.09)	undistorted

Table 4. Phlogopite compositions

	Olivine interface	Olivine interface	Mid-rim	Mid-rim	Melt interface	Melt interface	Melt interface
SiO_2	42.12 (17)	41.86 (17)	43.01 (17)	43.48 (17)	46.06 (18)	42.88 (17)	43.09 (17)
Al_2O_3	11.86 (9)	11.59 (9)	12.77 (9)	13.09 (10)	14.36 (10)	13.44 (10)	13.55 (10)
FeO	0.64 (9)	0.73 (9)	0.38 (7)	0.19 (7)	0.16 (7)	0.25 (7)	0.19 (7)
NiO	0.22 (3)	0.21 (3)	0.08 (3)	0.11 (3)	-	0.12 (2)	0.07 (3)
MgO	29.92 (15)	30.37 (15)	27.56 (15)	28.21 (15)	25.17 (14)	27.83 (15)	27.11 (15)
CaO	0.07 (1)	0.09 (1)	0.04 (1)	0.04 (1)	0.09 (1)	0.05 (1)	0.05 (1)
Na_2O	0.86 (8)	0.76 (7)	0.68 (7)	0.78 (7)	0.78 (7)	0.73 (7)	1.16 (8)
K_2O	8.70 (4)	8.62 (4)	9.33 (5)	9.28 (5)	8.18 (4)	9.56 (5)	9.34 (5)
Total	94.39	94.23	93.84	95.22	94.84	94.86	94.59
X (μm)	4	5	9	10	18	16	18
Si	2.95	2.94	2.95	3.006	3.143	2.982	3.002
Al	0.98	0.96	0.98	1.067	1.155	1.102	1.113
Fe	0.04	0.04	0.04	0.011	0.009	0.015	0.011
Ni	0.01	0.01	0.01	0.006	0.000	0.007	0.004
Mg	3.13	3.18	3.13	2.907	2.559	2.885	2.815
Ca	0.01	0.01	0.01	0.003	0.007	0.004	0.004
Na	0.12	0.10	0.12	0.105	0.103	0.098	0.157
K	0.78	0.77	0.78	0.818	0.712	0.848	0.830

Figure 1.

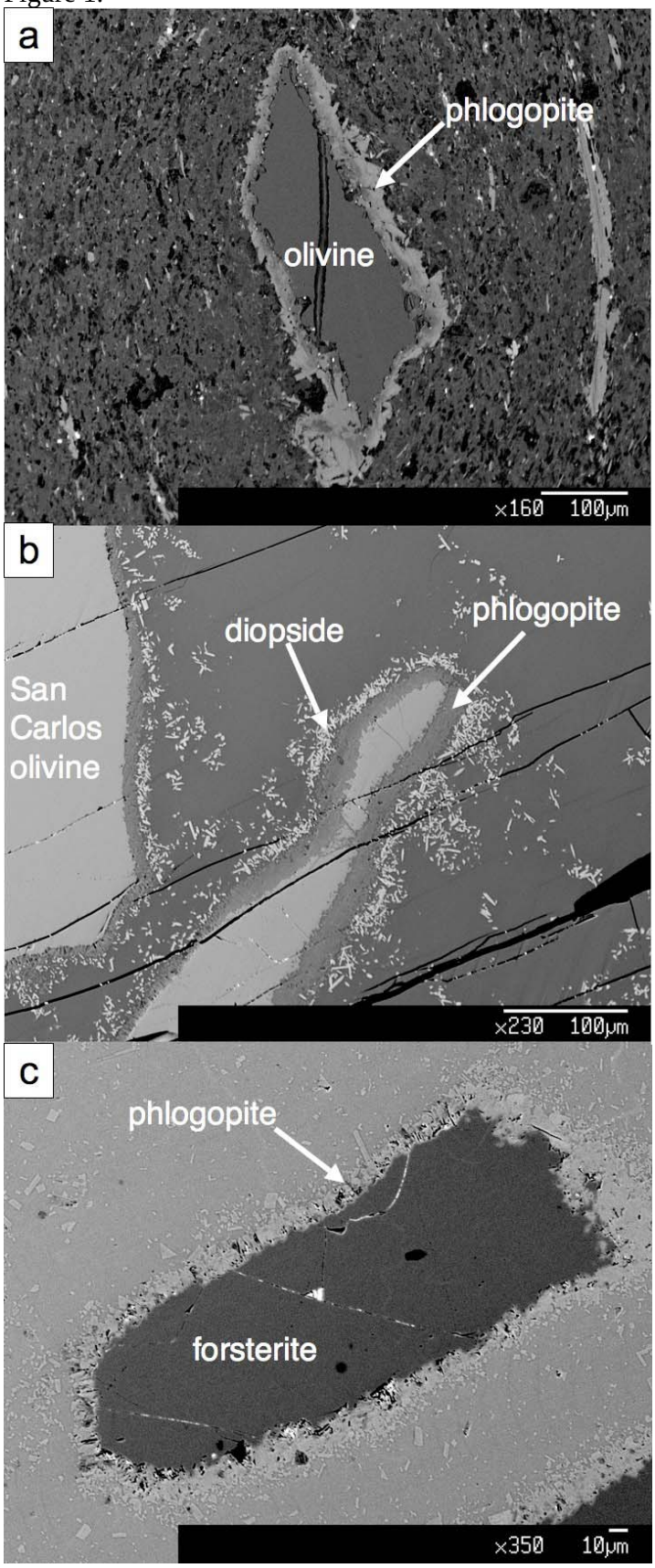
a
phlogopite
olivine
×160 100µm
b
diopside
phlogopite
San
Carlos
olivine
×230 100µm
c
phlogopite
forsterite
×350 10µm

Figure 2

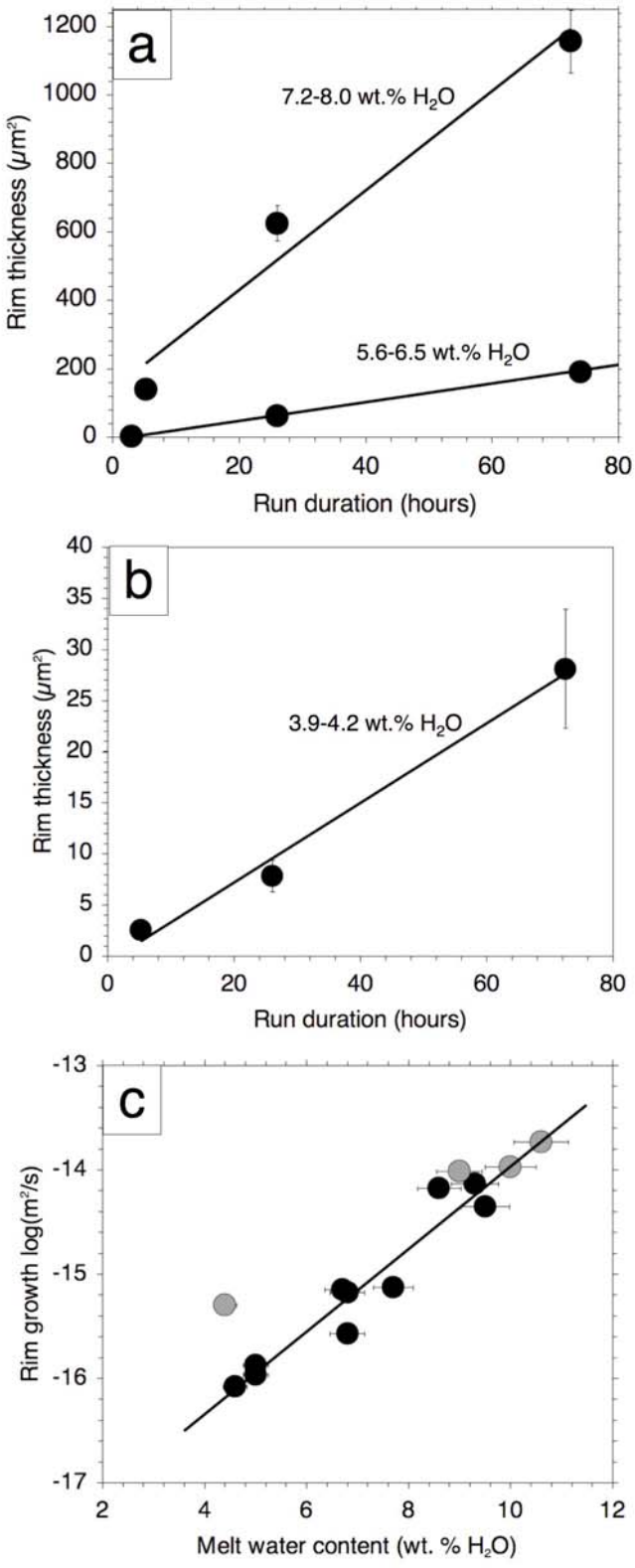
a
7.2-8.0 wt.% H_2O
5.6-6.5 wt.% H_2O
Rim thickness (μm^2)
Run duration (hours)
b
3.9-4.2 wt.% H_2O
Rim thickness (μm^2)
Run duration (hours)
c
Rim growth log(m^2/s)
Melt water content (wt. % H_2O)

Figure 3

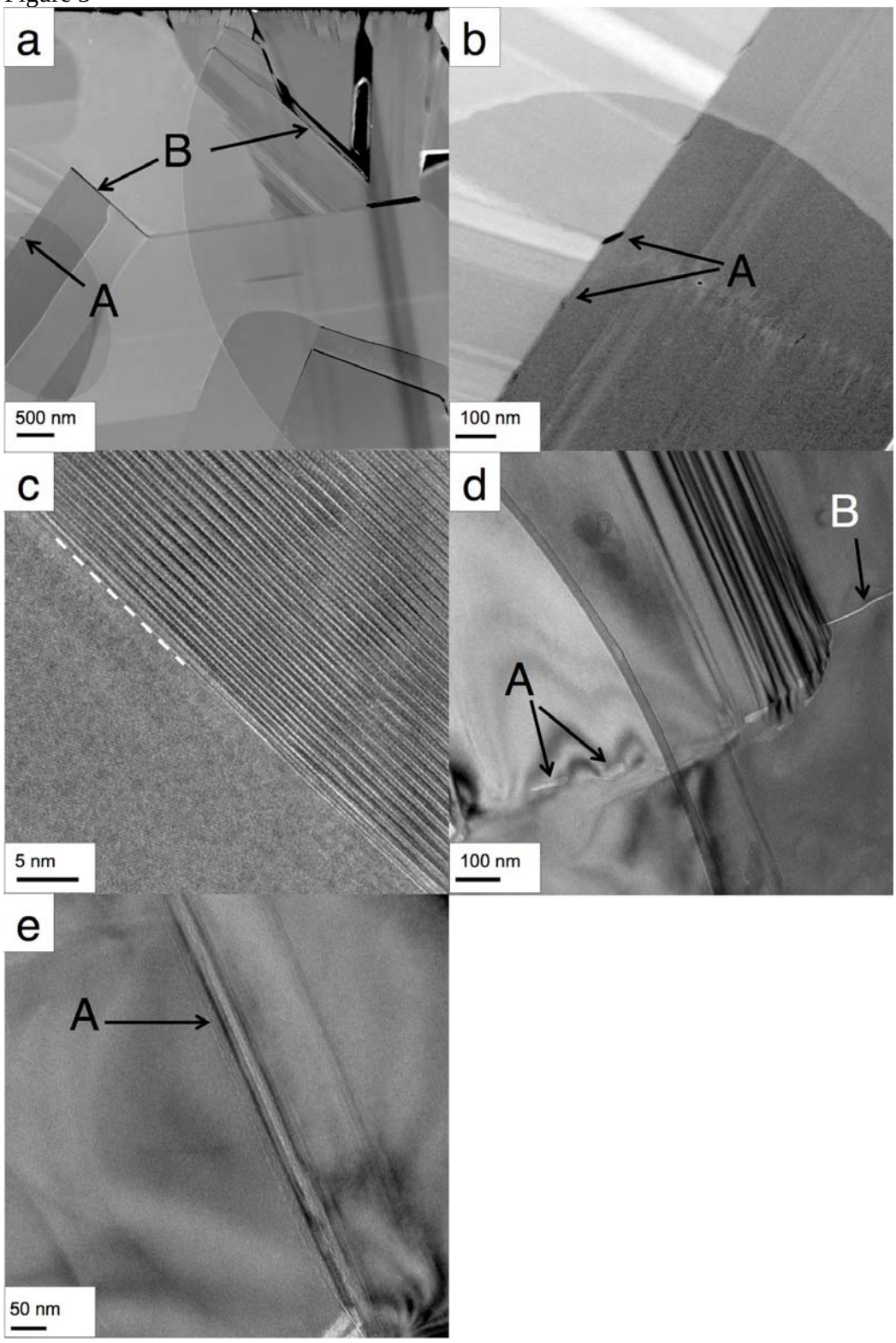

Figure 4

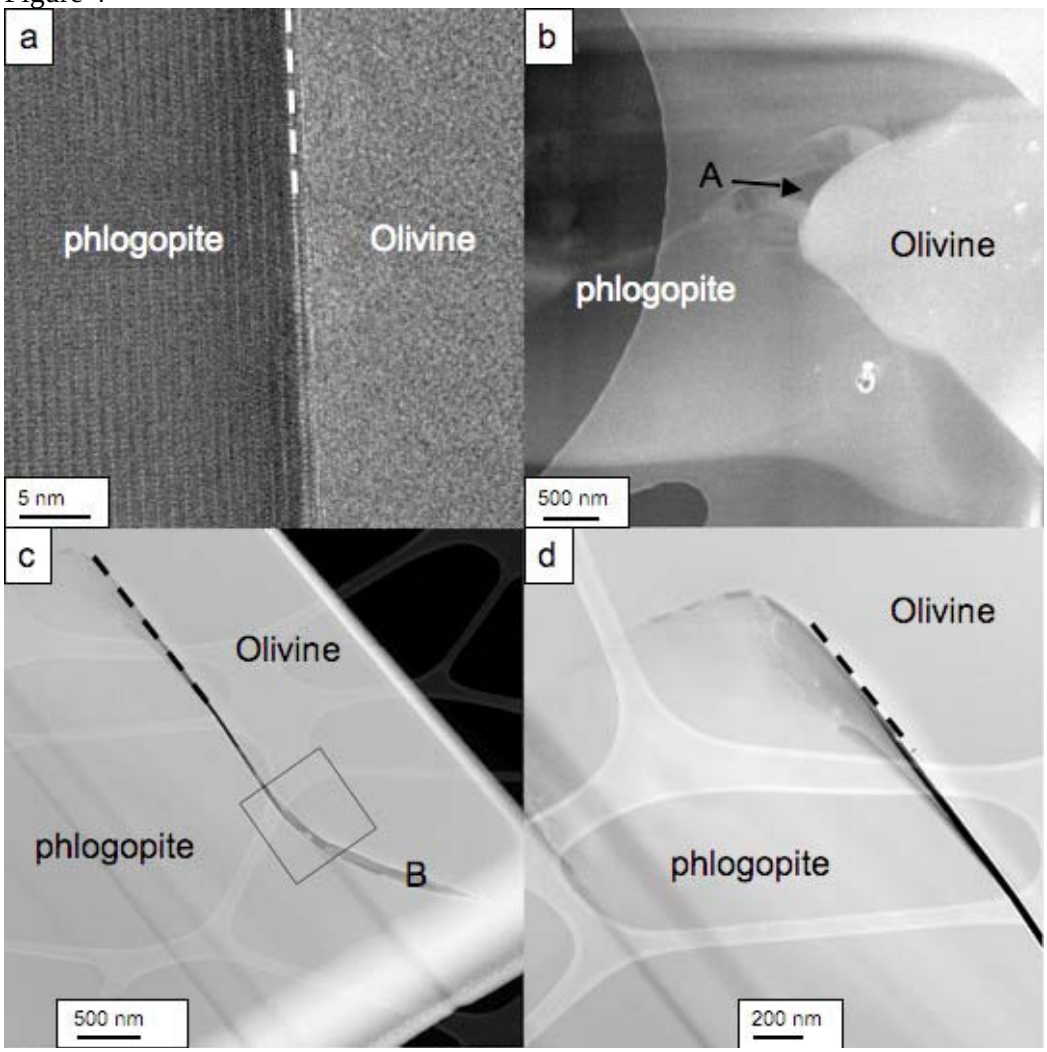
a
phlogopite
Olivine
5 nm
b
A
Olivine
phlogopite
500 nm
c
Olivine
phlogopite
B
500 nm
d
Olivine
phlogopite
200 nm

Figure 5

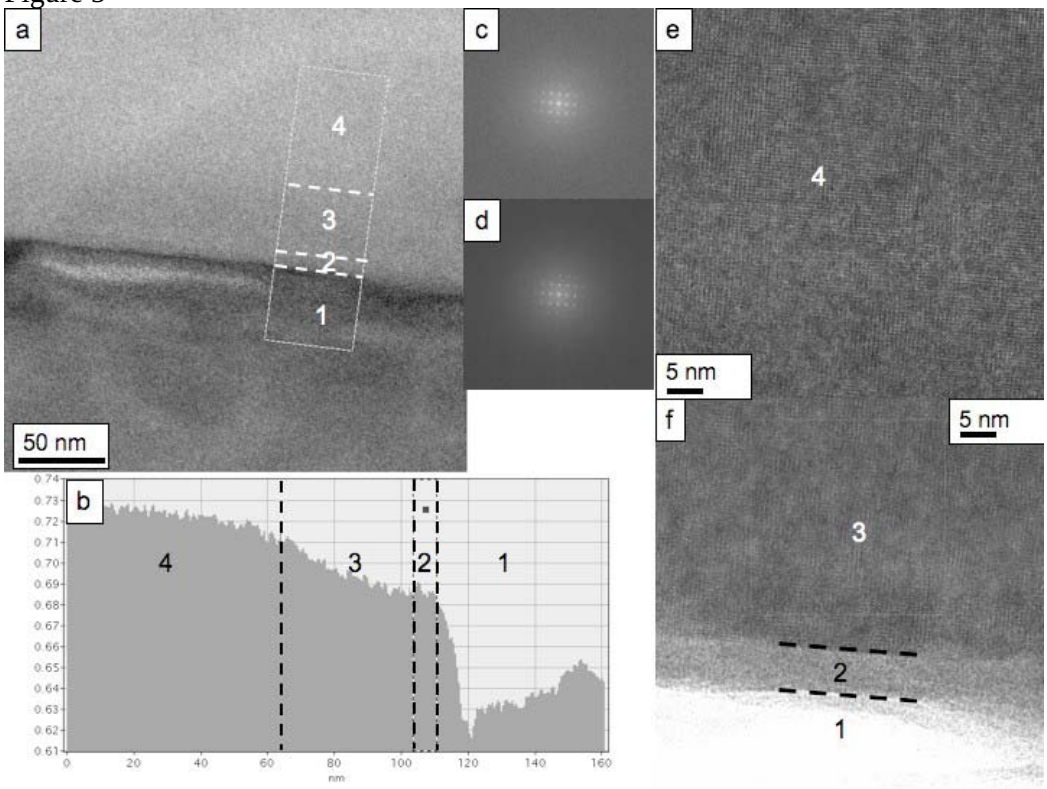
a
4
3
2
1
50 nm
c
d
e
4
5 nm
f
5 nm
3
2
1
b
4
3
2
1
0.74
0.73
0.72
0.71
0.70
0.69
0.68
0.67
0.66
0.65
0.64
0.63
0.62
0.61
0
20
40
60
80
100
120
140
160
nm

Figure 6

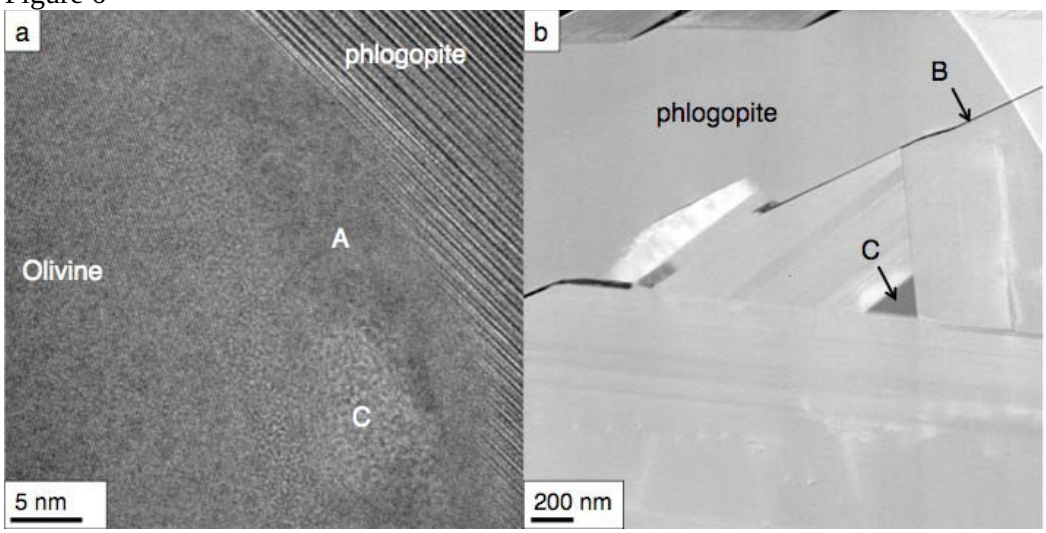

Figure 7

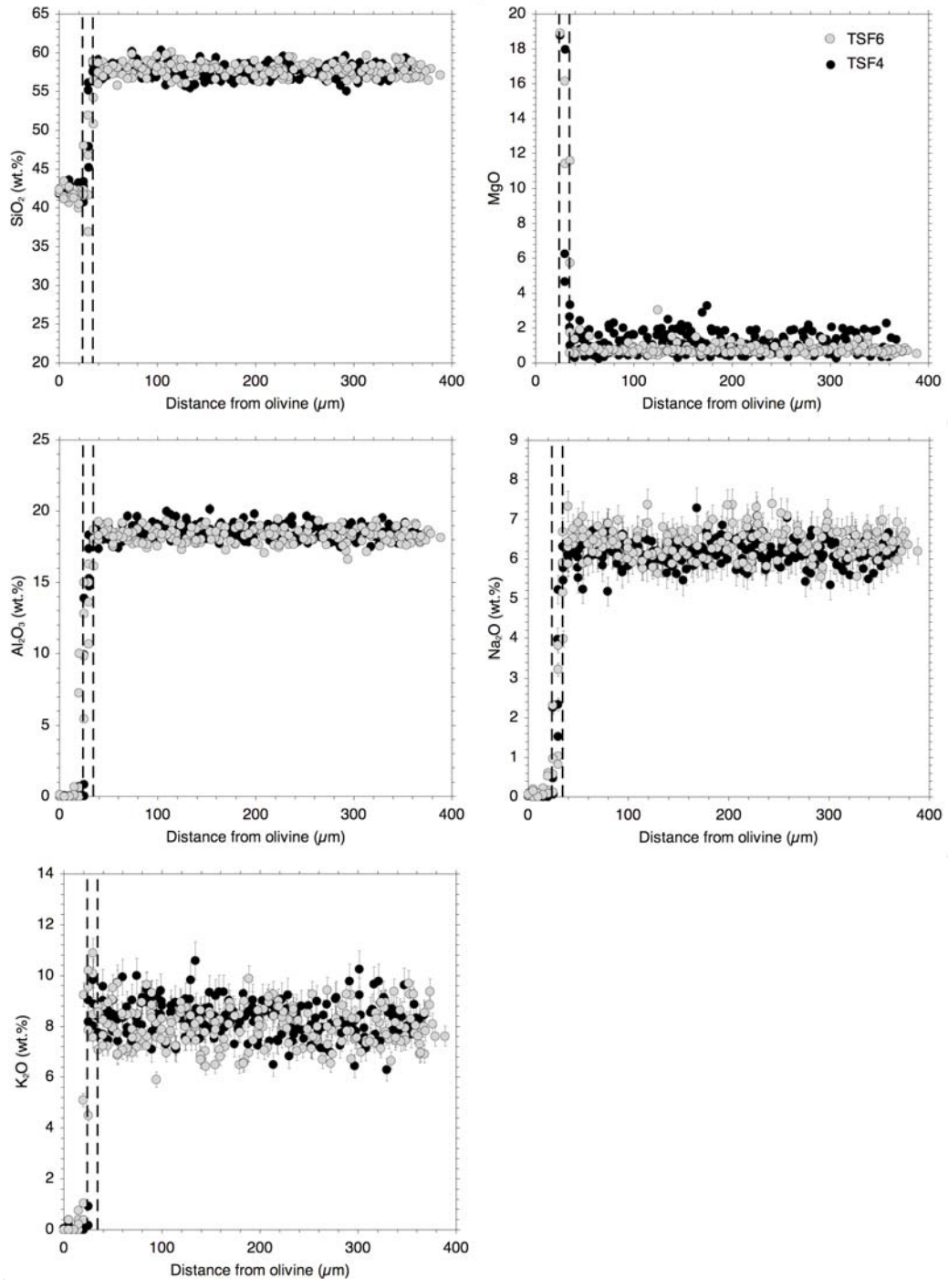
SiO2 (wt.%)
MgO
TSF6
TSF4
Al2O3 (wt.%)
Na2O (wt.%)
K2O (wt.%)
Distance from olivine (μm)

Figure 8

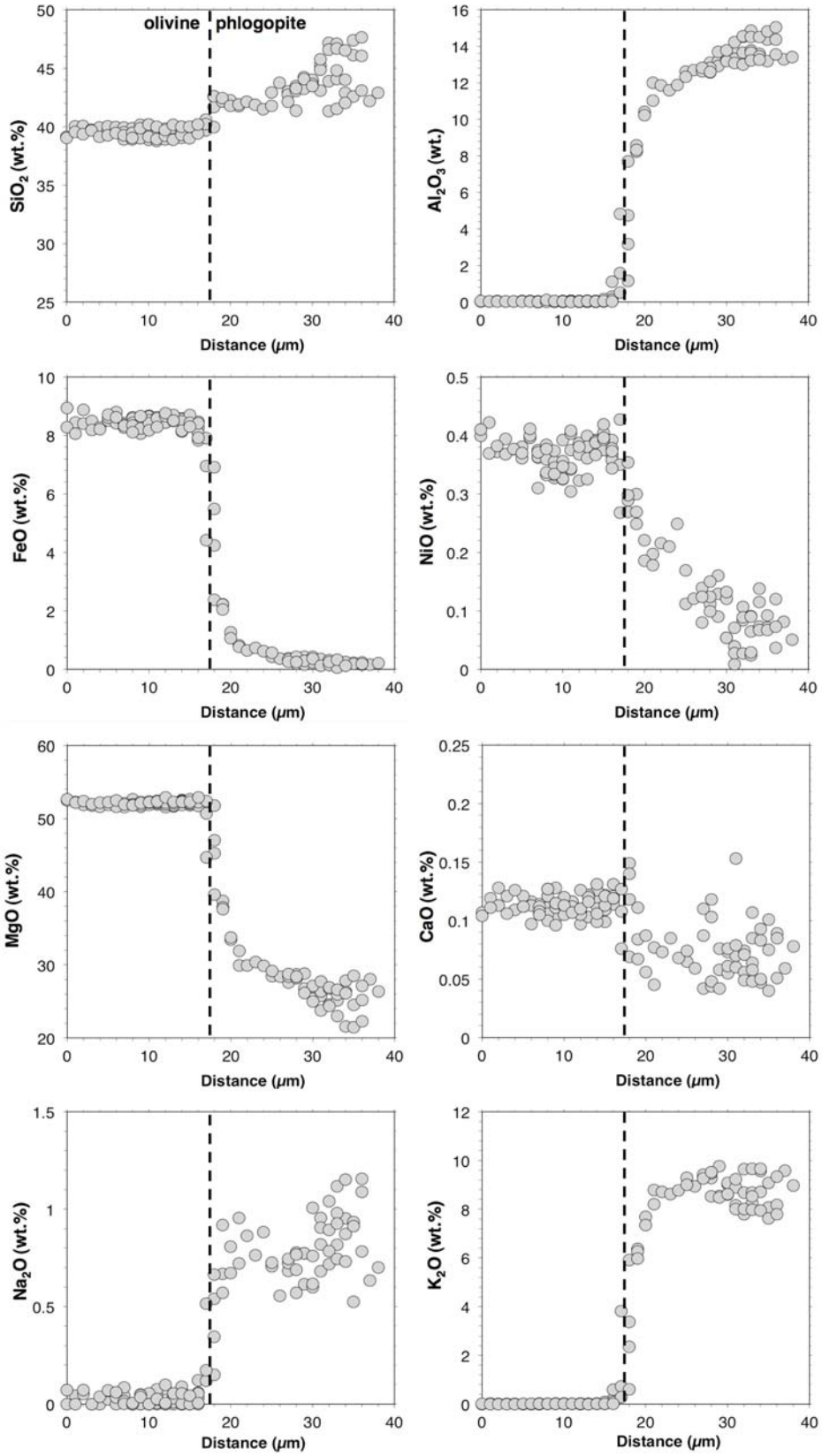
olivine
phlogopite
SiO2 (wt.%)
Al2O3 (wt.)
FeO (wt.%)
NiO (wt.%)
MgO (wt.%)
CaO (wt.%)
Na2O (wt.%)
K2O (wt.%)
Distance (μm)

Figure 9

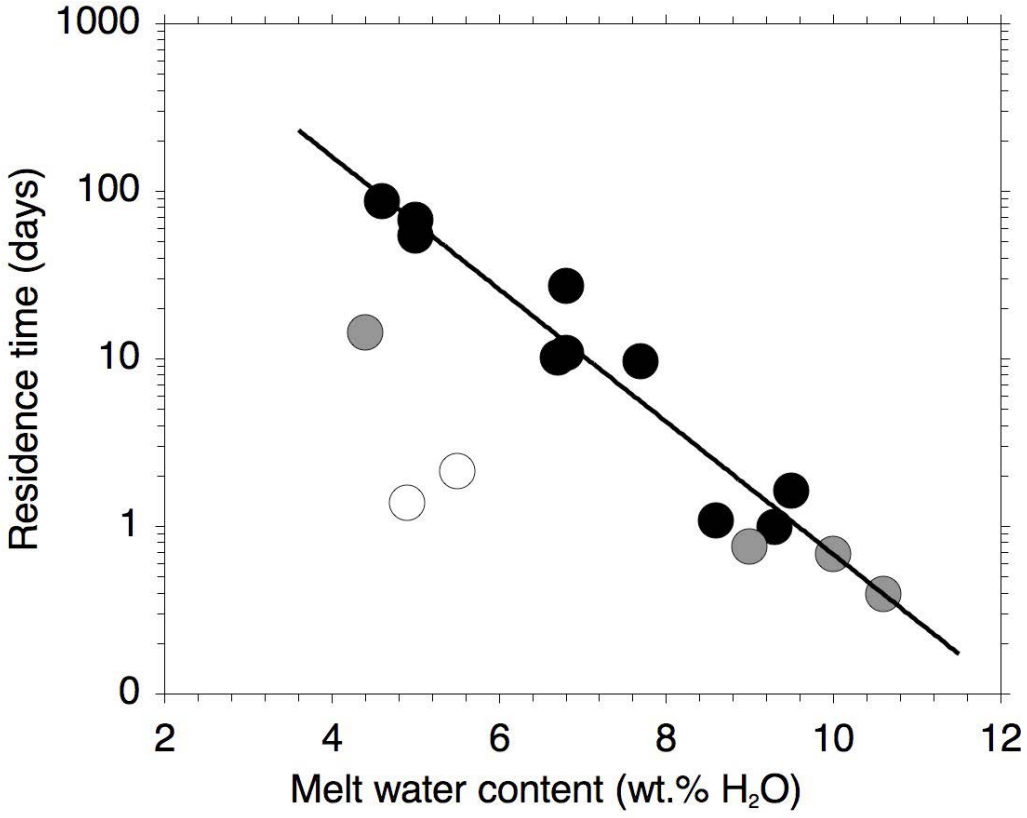
1000
100
10
1
0
Residence time (days)
2
4
6
8
10
12
Melt water content (wt.% H_2O)